Carrier orbit coupling in stage-2 IBr graphite

1997 J. Phys.: Condens. Matter 9 8221

(http://iopscience.iop.org/0953-8984/9/39/008)

J. Phys.: Condens. Matter **9** (1997) 8221–8235. Printed in the UK PII: S0953-8984(97)83268-7

Carrier orbit coupling in stage-2 IBr graphite

E Tcherner, P K Ummat and W R Datars

Department of Physics and Astronomy, McMaster University, Hamilton, Ontario, Canada L8S 4M1

Received 9 June 1997

Abstract. The electronic properties of the stage-2 IBr graphite intercalation compound were investigated by means of the de Haas–van Alphen (dHvA) effect. Thirty dHvA frequencies were found with the magnetic field parallel to the *c*-axis. These results are explained by the Fermi surface model formed by zone folding resulting from commensurate ($\sqrt{1}83R26.33^\circ \times 2\sqrt{3}R0^\circ$) in-plane superlattice translations which coupled carrier orbits. The unfolded Fermi surface was the primitive two-dimensional Fermi surface of Blinowski *et al* for graphite intercalation compounds. By adjusting the dimensions of this Fermi surface, all the dHvA frequencies were interpreted with an accuracy of ≈5%. The Fermi radii of the unfolded Fermi surface were $k_1 = 0.118$ Å^{-1} and $k_2 = 0.183$ Å^{-1}. The dHvA frequencies (455 and 1106 T) were used to determine the band parameters γ_0 (the interaction of nearest neighbours) and γ_1 (the interaction of nearest layers) in Blinowski's theoretical band model for acceptor-type graphite intercalation compounds.

1. Introduction

Graphite intercalation compounds (GICs) formed with halogen molecules such as Br_2, ICl, and IBr are considered as a class within the large family of acceptor-type GICs [1]. This classification stems from the observation of intercalation and de-intercalation of seemingly unchanged halogen molecules, driven only by the external halogen vapour pressure and temperature, with the Br_2 GICs as the most studied system. The ($hk0$) x-ray diffraction, electron diffraction [2] and x-ray absorption spectroscopy studies [3, 4] established that the ICl and IBr molecules form a commensurate superlattice with lattice parameters of ($\sqrt{1}83R26.33^\circ \times 2\sqrt{3}R0^\circ$) with respect to the graphite lattice vectors at room temperature. The ^{129}I Mössbauer study of stage-2 ICl and IBr GICs [5] supported this model of the intercalate structure derived from x-ray absorption (EXAFS) studies [4] of these systems.

In recent years, the physical properties of the ICl GIC including the *c*-axis resistivity [6], the *a*-axis conductivity and the Hall coefficient [7], specific heat [8], and *c*-axis thermoelectric power [9] have been studied extensively. The ICl GICs were reported to be fragile during cooling and heating even in the low-temperature range. The structural transition in which the commensurate, in-plane superlattice is formed takes place at 305 K in the stage-1 ICl GIC and at 311 K in the stage-2 ICl GIC, corresponding to the observed anomalies in the heat capacity [10]. The temperature dependence of the *c*-axis resistivity of stage-1 and 2 ICl GICs demonstrates an ordering phase transition at the same temperatures [6]. However, the IBr GIC remains the least studied of the compounds with the halogen molecules.

Therefore, this work will focus on the graphite intercalation compound with iodine monobromide, namely the stage-2 IBr GIC, with measurements of the de Haas–van Alphen

0953-8984/97/398221+15$19.50

(dHvA) effect. The dHvA effect can be observed in pure metals and dilute alloys at low temperatures and high magnetic fields. Fermi surface sizes, cyclotron masses, Dingle temperatures and density of carriers can be obtained directly from the experiment. Measurements of the dHvA effect yield extremal cross-sectional Fermi areas which are perpendicular to the applied magnetic field direction.

The number of dHvA frequencies observed in a stage-n GIC in excess of the n frequencies arising from the n π bands can result from the presence of an in-plane intercalant superlattice. The commensurate intercalant superlattice with respect to the underlying carbon hexagonal lattice can create additional Fermi surface pieces due to zone-folding effects introduced by the additional periodicity of the intercalant. The symmetry of the GIC is assumed to be the same as pristine graphite and the effect of the superlattice periodicity is treated as a perturbation. Zone folding is the translation by the intercalant reciprocal lattice vectors of the large Brillouin zone of graphite on to the smaller zone of the intercalant. It couples carrier orbits. In this reduced zone scheme, the constant curvature orbits formed by the Fermi surface overlap give rise to additional dHvA frequencies. Thus, the dHvA effect effectively probes the two periodicities. It is a way of determining the superlattice and its effect on the Fermi surface.

The zone-folding effect has been detected experimentally in stage-1 $InCl_3$ GIC [11], stage-2 $InCl_3$ GIC [12] and stage-2 $SbCl_5$ GIC [13]. For the stage-2 $InCl_3$ GIC [12] the dHvA frequencies were in the range 126–1424 T and the cyclotron masses were between 0.095 and 0.27 m_0. There were at least 15 dHvA frequencies observed. All of the frequencies except one were explained by the zone folding of the Fermi surface by the superlattice of the ordered intercalant. The superlattice periodicity was $8\sqrt{3} \times 8\sqrt{3}R30^\circ$ with respect to the graphite lattice. For the stage-2 $SbCl_5$ GIC [13], forty dHvA frequencies were observed. The results were used to test the Fermi surface model resulting from the commensurate $14 \times 14R30^\circ$ in-plane superlattice truncations of the primitive 2D Fermi surface of the theoretical band model for acceptor-type GICs. By adjusting the dimensions of this Fermi surface, all of the dHvA frequencies were interpreted with an accuracy of 5%.

The experimental results obtained with apparatus which has been described previously [11] are given in section 2. The analysis using zone folding is described in section 3. The conclusions and an assessment of the results with respect to their implications for the dHvA effect are in section 4. The purpose of this work is to present electronic properties of the stage-2 IBr GIC and to show the dramatic effects of the IBr periodicity by coupling orbits on the Fermi surface. It illustrates clearly the interplay of two periodicities and provides an experimental base for the theoretical understanding of zone folding.

2. Results

Five samples were made in order to carry out a thorough investigation of the stage-2 IBr GIC. There were some differences in the preparation processes and in the treatment before extensive measurements with different samples.

Samples 1 and 2 were prepared in sealed reaction tubes heated to a temperature of 55 °C for 15 d. Sample 3 was prepared in a sealed reaction tube heated at 55 °C for the first 15 d and then heated at a temperature of 60 °C for the next 7 d. In all three cases the reaction tubes were opened immediately after sample preparation. Samples 2 and 3 remained inside a dry box and sample 1 was exposed to air after x-ray diffraction measurements for the experiment. The samples were cooled very slowly between room temperature and liquid nitrogen temperature (about 3 d) in order to eliminate possible cracking of the samples and possible complications of the dHvA spectrum due to this factor. Measurements were

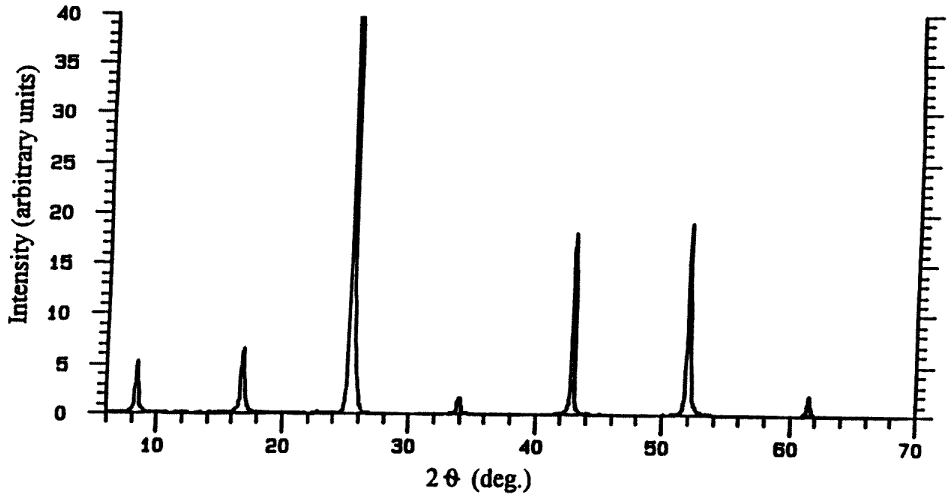

(*a*)

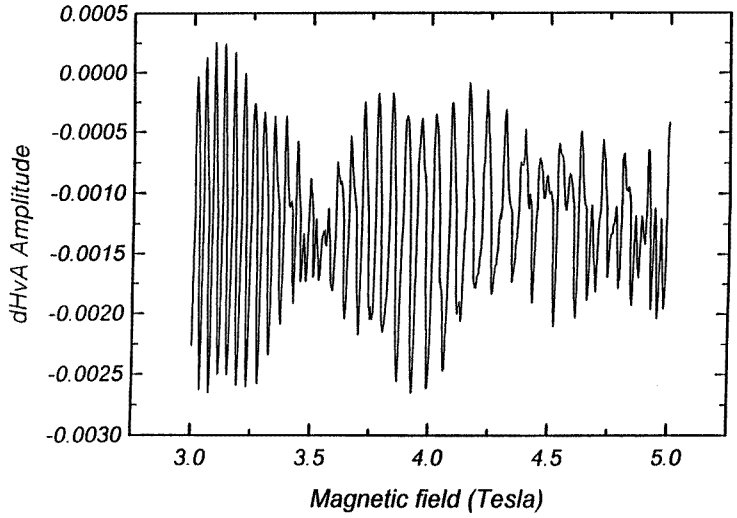

(*b*)

Figure 1. (a) The x-ray (00*l*) diffraction of sample 4 with Cu K_2 radiation; (b) dHvA oscillations of the stage-2 IBr GIC sample 2.

performed at different temperatures between 1.5 and 4.2 K, in many different magnetic field ranges varying from 1 T up to 8 T, with different dHvA spectrum resolutions (with the best resolution of 1.25 T between consecutive points).

Samples 4 and 5 were prepared in sealed reaction tubes heated to a temperature of 55 °C for 15 d. They remained inside the sealed reaction tubes at room temperature for a period of 1 month after preparation. The samples were left inside the sealed reaction tubes in order to keep them in an IBr vapour pressure. Each one was placed into the sealed cell inside a dry box, and therefore was never exposed to air. The probe with a sealed sample cell was

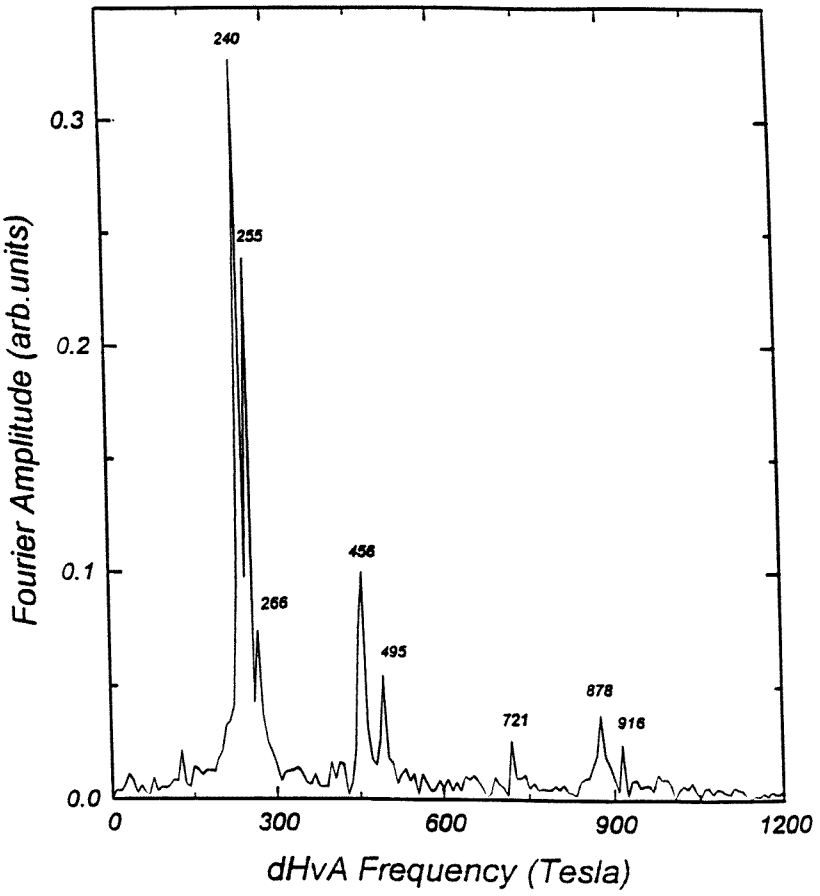

Figure 2. The Fourier transform spectrum of the dHvA oscillations of samples of stage-2 IBr GIC.

lowered slowly (over 16 h) into the precooled experimental station. With this technique, the dHvA measurements of sample 4 were performed within 24 h after the sealed reaction tube was opened. After a complete set of measurements of sample 5, it was exposed to air for 7 d and measured again.

The sample conditions are summarized in table 1. The most significant condition that affected the data was whether the sample was kept in the reaction tube until just before the experiment. Air exposure was also important.

The (00l) x-ray diffraction spectrum of sample 4 shown in figure 1 is typical of all samples and reveals a single-staged sample with no visible diffraction from other stages or graphite. The narrow diffraction peaks indicate good sample homogeneity. There is no evidence of stage disorder that could affect the data. The repeat distance I_c determined from the slope of the best-fit line of a plot of reflection order l versus $1/d_l$ where d_l is the d-spacing for reflection order l is 10.53 Å. This value is similar to the value of 10.43 Å determined previously [6].

The air sensitivity of sample 1 was investigated by (00l) x-ray diffraction when it was not exposed to air and after air exposure for 3, 7, 14, 30 and 60 d. The x-ray spectrum

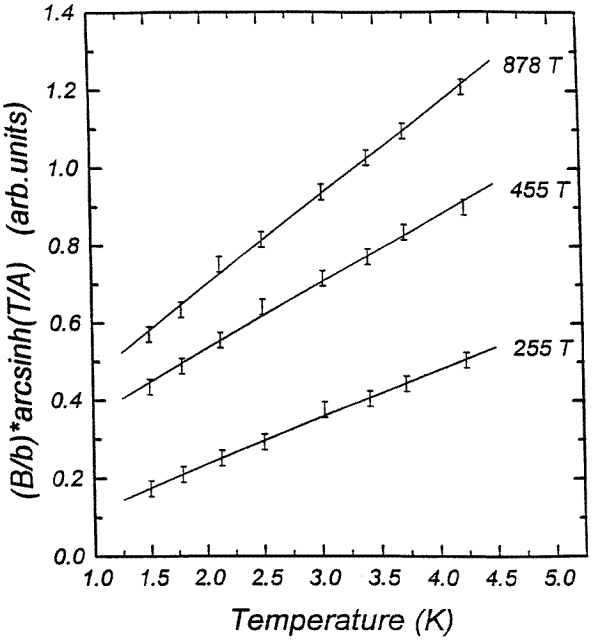

Figure 3. The temperature dependence of $\sinh^{-1}(T/A)$ for frequencies of 255, 455 and 878 T, where A is the amplitude of the corresponding frequency of sample 2.

Table 1. Conditions for the IBr GIC samples.

Sample number	Preparation temperature (°C)	Time in tube after the reaction	Air exposure
1	55	1 d	yes
2	55	1 d	no
3	55 and 60	1 d	no
4	55	1 month	never
5	55	1 month	never for first, 7 d for second measurement

remained the same in all the tests, indicating that the staging is not affected by air exposure. The recorder trace of the dHvA oscillations of sample 2 shown in figure 1 has good signal at low fields, indicating good sample quality. However, there are oscillations with different frequencies.

The Fourier transform spectrum for sample 2 in figure 2 indicates at least eight frequencies. In addition there was a small peak at 123 T which was the largest from samples 4 and 5. For samples 1–3 peaks at 240 and 255 T always dominated with the greatest amplitudes. Whenever the measurement was performed at lower resolution, the peaks at 240, 255 and 266 T merged into a single peak at 247 T with even greater common amplitude. The frequency $f_1 = 455$ T is identified as the first of the two frequencies expected from the graphitic bands of the stage-2 GIC. The cross-sectional Fermi area determined by the relation $A_f = (4\pi^2 e/h) f$ is $A_1 = 0.0434$ Å^{-2} and the Fermi values ($k_1 = 0.118$ Å^{-1}).

The carrier cyclotron masses corresponding to these frequencies were determined from

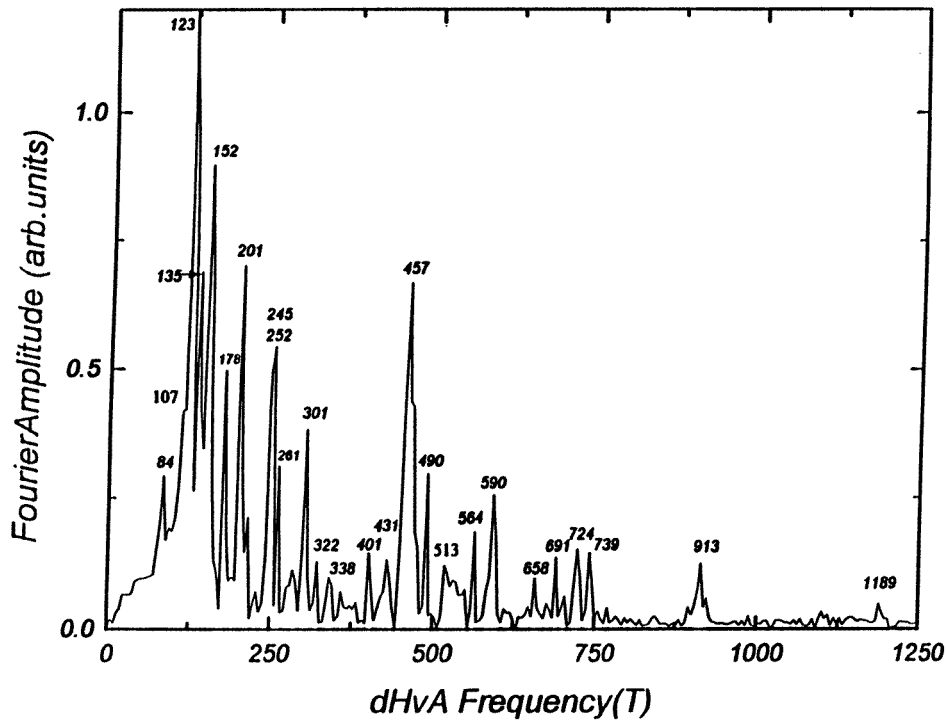

Figure 4. The Fourier transform spectrum of the dHvA oscillations of sample 4 of the stage-2 IBr GIC.

the temperature dependence of the dHvA amplitude between 1.5 and 4.2 K with the *c*-axis parallel to the magnetic field direction. The dHvA amplitude is related to the sample temperature by the proportionality

$$A \propto T/\sinh\left(bm^*T/Bm_0\right) \tag{1}$$

where A is the dHvA amplitude at temperature T and magnetic field B; m^* and m_0 are the cyclotron mass and the free electron mass, respectively, and $b = 2\pi^2 k_B cm/he = 14.69\ \mathrm{T\ K^{-1}}$ is a universal constant. Because all the constants are intrinsically included in the plot, the ratio m^*/m_0 can be determined numerically as the slope of the best-fit line for the plot $(B/b)\ \sinh^{-1}(T/A)$ versus T since

$$m^* = (B/bT)\sinh^{-1}(T/A)m_0. \tag{2}$$

Figure 3 shows a plot of the experimentally obtained data points and the best-fit lines for the frequencies 255, 455 and 878 T. The temperature dependent measurements were performed at eight different temperatures in order to provide values for the carrier cyclotron masses.

The results are

$m^* = (0.115 \pm 0.005)\ m_0$	for 240 T	$m^* = (0.175 \pm 0.005)\ m_0$	for 495 T
$m^* = (0.12 \pm 0.005)\ m_0$	for 255 T	$m^* = (0.20 \pm 0.005)\ m_0$	for 724 T
$m^* = (0.125 \pm 0.005)\ m_0$	for 264 T	$m^* = (0.23 \pm 0.005)\ m_0$	for 878 T
$m^* = (0.16 \pm 0.005)\ m_0$	for 455 T	$m^* = (0.235 \pm 0.005)\ m_0$	for 916 T.

Table 2. dHvA frequencies compared to values calculated by circle construction using the low- (455 T) and high-frequency (1106 T) bands. (U) denotes an uncoupled orbit.

dHvA (T)	Calculated frequency (T)	Difference (%)	Construction
	9.4(U)		F9
	11.0(U)		F8
	43.1(U)		
	79.7		F4
84	85.8(U)	2.1	F7
95	93.8	−2.3	F3+F4
107	107.9(U)	0.8	2F3+F4
124	128.6	3.7	F1+F3+F4
136	142.7	4.7	F1+2F3+F4
152	157.8	3.7	F2+F4
	171.9		F2+F3+F4
177	177.5	0.3	2F1+2F3+F4
201	206.7	2.8	F1+F2+F3+F4
240	235.8(U)	−1.8	2F2+F4
254	249.9	−1.6	2F2+F3+F4
263	264.0	0.4	2F2+2F3+F4
302	305.5	1.1	2F1+2F2+F4
322	322.4(U)	0.1	F2+F3+F4+F5
339	336.5	−0.7	F2+2F3+F4+F5
357	357.2	0.0	F1+F2+F3+F4+F5
400	400.5	0.1	2F2+F3+F4+F5
431	435.3	0.9	F1+2F2+F3+F4+F5
494	496.2(U)	0.5	2F1+F2+F3+F4+F6
513	510.3	−0.5	2F1+F2+2F3+F4+F6
565	565.1	0.0	2F2+2F3+F4+2F5
589	588.4	−0.1	2F1+2F2+2F3+F4+F6
658	660.8	0.4	2F1+F2+2F3+F4+F5+F6
691	695.6	0.6	3F1+F2+2F3+F4+F5+F6
721	724.8	0.5	2F1+2F2+F3+F4+F5+F6
740	738.8	−0.2	2F1+2F2+2F3+F4+F5+F6
879	875.3	−0.4	2F1+2F2+2F3+F4+2F5+F6
916	912.7	−0.4	4F1+2F2+2F3+F4+2F6
1057	1063.2	0.6	4F1+2F2+2F3+F4+F5+2F6
1189	1199.7	0.9	4F1+2F2+2F3+F4+2F5+2F6

The angular dependence of the dHvA frequency can give insight into the shape of the Fermi surface. The angular dependence of the dHvA frequency f_θ from a straight cylinder of the Fermi surface is $f_\theta = f_0 \sec\theta$, where θ is the angle between the magnetic field direction and the axis of the straight cylinder, and f_0 is the frequency at $\theta = 0^\circ$. If the cylinder is undulating, there are two frequencies at $\theta = 0^\circ$ from the minimum and maximum cross-sections of the undulating cylinder. These two frequencies merge as the angle θ increases and the areas of the two cross-sections approach each other.

The test revealed the two-dimensional dependence of the Fermi surface cylinders for frequencies 240, 255, 455, 495 and 916 T, with no merging of the frequencies 240 and 255 T. The angular range for the observation of the oscillation was limited to $\theta \leqslant 22^\circ$, because of the scattering of the carriers from their cyclotron orbits by the intercalant layers for larger values of θ. The cylindrical shape of the Fermi surface was determined for $0^\circ \leqslant \theta \leqslant 22^\circ$, although the complete shape of the Fermi surface could not be derived.

The Fourier transform frequency spectrum of the dHvA oscillations for sample 4 is

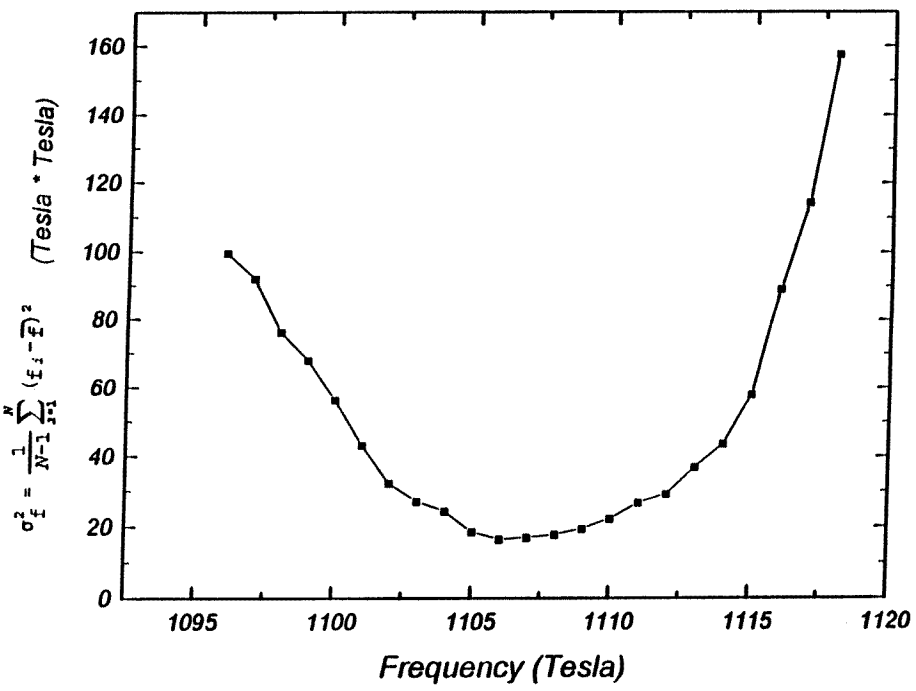

Figure 5. The sum of the mean square deviation of the individual measurements from the mean value for the fundamental frequency f_2, plotted as a function of f_2.

shown in figure 4. There are 27 frequencies at 84, 107, 123, 135, 152, 178, 201, 245, 252, 261, 301, 322, 338, 357, 401, 431, 457, 490, 513, 564, 590, 658, 691, 724, 739, 913 and 1189 T. The frequency spectrum includes all the frequencies (except 878 T) that were seen with samples 1–3. This time the most prevalent peak is at 123 T. Peaks at 245, 252 and 261 T have medium amplitudes. The Fourier transform frequency spectrum of the dHvA oscillations for sample 5 was very similar to the spectrum of sample 4. Table 2 presents average values from all the samples of the dHvA frequencies.

Sample 5, which had not been previously exposed to air, was exposed to air for 7 d and measured again in exactly the same experimental conditions. Certain changes were noticed in the new Fourier transform frequency spectrum. All the frequencies typical of samples 1–3 were observed: 240, 255, 264, 455, 495, 724, 878 and 916 T. A characteristic splitting of frequencies 240, 255 and 264 T was seen distinctly. Frequencies 322, 338, 357, 401, 431, 564, 590, 658 and 691 T were not observed or their amplitudes were too weak to be recorded. Thus, some dHvA frequency branches disappear after air exposure of a sample.

3. Analysis and discussion

The hole carriers in a stage-2 graphite intercalation compound, are in two energy bands and are located at the corners of the hexagonal Brillouin zone of the graphite lattice. They are in Fermi-surface cylinders directed along the *c*-axis. The cross-sectional areas of the cylinders are small relative to the area of the hexagonal surface of the Brillouin zone.

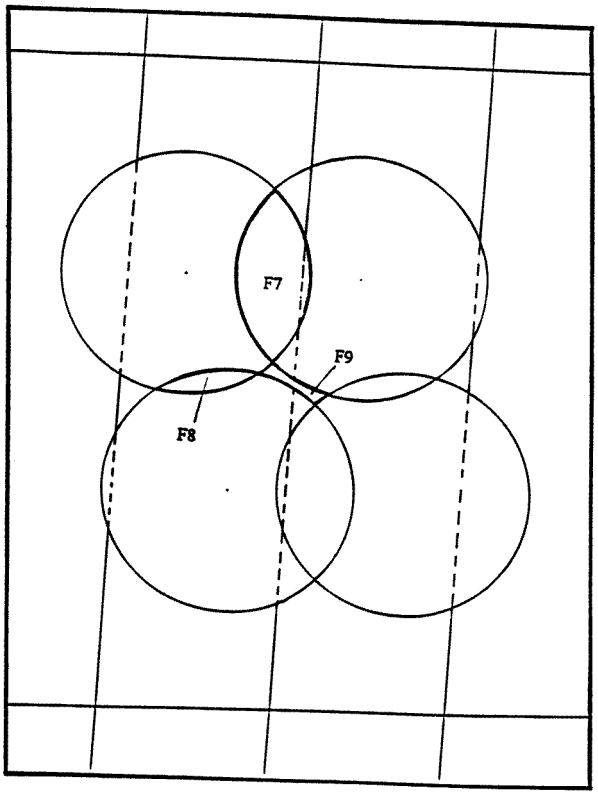

Figure 6. The circle construction for the low-frequency band (455 T).

When the intercalant molecules have an ordered arrangement they form a superlattice on the hexagonal carbon arrangement with a much smaller Brillouin zone. When the Fermi surface is translated by the reciprocal lattice vectors of the superlattice, there are overlaps of the Fermi surface from neighbouring translations, which permit the coupling of the carrier orbits.

The ($hk0$) x-ray diffraction, electron diffraction and x-ray absorption spectroscopy studies indicate that the IBr molecules form a commensurate superlattice with lattice parameters of ($\sqrt{1}83R26.33^\circ \times 2\sqrt{3}R0^\circ$) with respect to the graphite lattice vectors at room temperature [2–4]. This commensurate superlattice allows for the reciprocal space translation of the cylindrical graphite Fermi surface located at the U and U′ points of the graphite Brillouin zone to the O and O′ points of the intercalant Brillouin zone. It is the overlap of these cylinders from different translations that enables the determination of the zone folding of the fundamental dHvA frequencies into many frequencies.

It is necessary to use the band frequencies f_1 and f_2 of the graphitic bands of the stage-2 GIC (and the corresponding cross-sectional Fermi areas, determined by the relations $A_1 = (4\pi^2 e/h) f_1$ and $A_2 = (4\pi^2 e/h) f_2$. The analysis involves testing different frequencies in order to find the Fermi surface construction which agrees with the experimentally determined Fermi surface pieces. The determination of these orbits was made by drawing the fundamental orbits (circles in two dimensions with radii $k_1 = \sqrt{A_1}/\pi$ and $k_2 = \sqrt{A_2}/\pi$) at the O and O′ points of the first, second and third Brillouin zones of

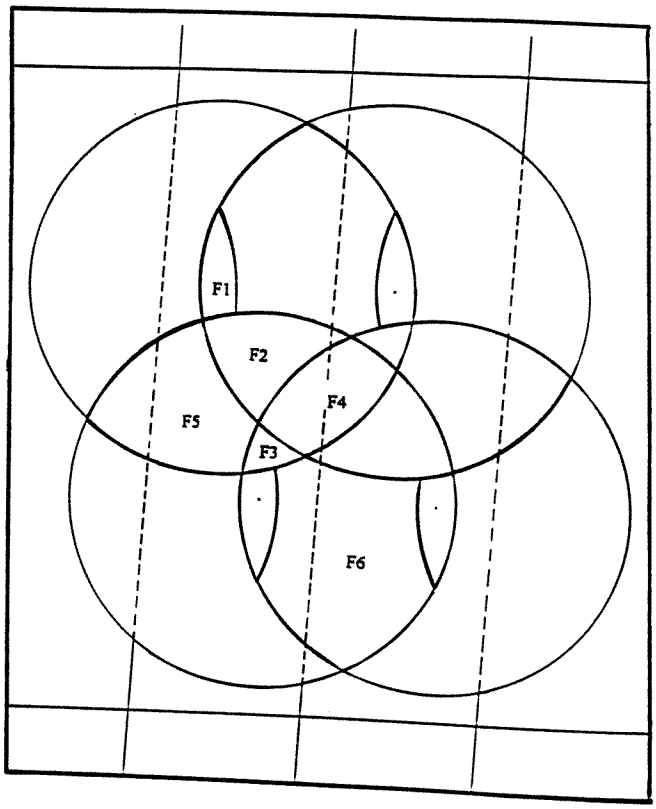

Figure 7. The circle construction for the high-frequency band (1106 T).

the intercalant superlattice.

When the ($\sqrt{1}83R26.33^\circ \times 2\sqrt{3}R0^\circ$) superlattice was used there was no way to explain the frequencies observed because the size of the intercalant Brillouin zone was much too large with respect to any reasonable fundamental frequency to provide the overlap of circles from neighbouring Brillouin zones. However, with the magnitude of the intercalant lattice vectors doubled, the size of the Brillouin zone shrinks by one-half and provides sufficient overlap to adjust the sizes of the circles to fit the dHvA data.

The resulting cross-sectional areas were calculated analytically by computer simulation of the model. Striking agreement was achieved with the fundamental frequency $f_2 = 1106$ T ($A_2 = 0.106$ Å^{-2} and $k_2 = 0.183$ Å^{-1}). The sum of the mean square deviations of the individual measurements from the calculated values is plotted as a function of f_2 in figure 5. It demonstrates the sensitivity of the choice to any deviations from $f_2 = 1106$ T and shows that $f_2 = 1106$ T is the local minimum. The plot accounts for all experimentally observed frequencies except 84 T for the sample unexposed to air. No close agreement was found for any other frequency in the range from 750 to 1600 T.

The frequency $f_1 = 455$ T was identified as the first of the two frequencies expected from the graphitic bands of the stage-2 GIC. The cross-sectional Fermi area is $A_1 = 0.0434$ Å^{-2} with $k_1 = 0.118$ Å^{-1}. This frequency was chosen for three reasons. First, it is one of the observed frequencies from the dHvA data. Second, this frequency always dominates in its neighbourhood. The third reason arises from an analysis of the zone folding

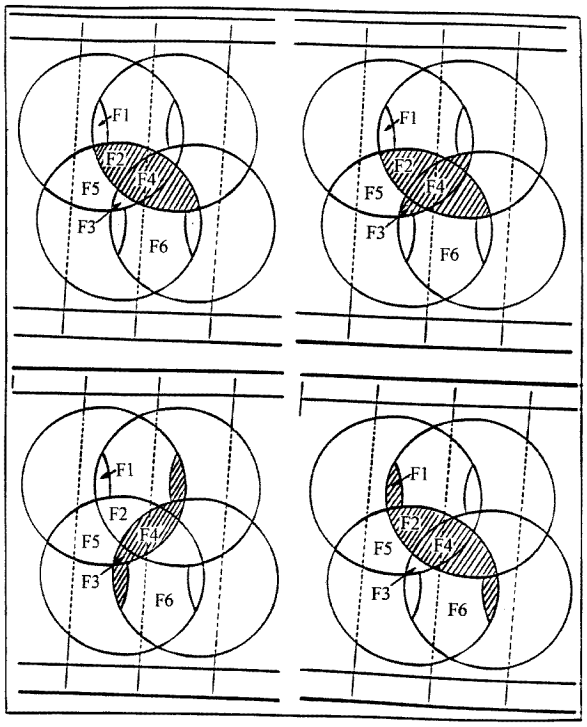

Figure 8. The circle construction showing coupled and uncoupled orbits (1106 T) corresponding to the 236, 264, 178 and 306 T frequencies.

of the frequency 455 T. The overlap of the frequency results in an uncoupled carrier orbit with a frequency of 84 T, which is repeatedly observed in the dHvA frequency spectrum.

The choice of the fundamental frequencies $f_1 = 455$ T and $f_2 = 1106$ T is in agreement with previous work on stage-2 $SbCl_5$ [14] intercalated graphite (where the two fundamental frequencies are $f_1 = 422$ T and $f_2 = 1102$ T) and on stage-2 $InCl_3$ GIC [12] for which $f_1 = 467$ T and $f_2 = 1320$ T.

The overlaps of the orbits in the first, second and third Brillouin zones are shown in figures 6 and 7 for f_1 and f_2, respectively. From figure 6, there are three pieces F7 (85.8 T), F8 (11 T) and F9 (9.4 T) that result from the overlap of circles for the lower frequency. These pieces can be coupled together to allow for extended orbits through reciprocal space. However, only a piece consisting of one type of curvature can be a carrier orbit. The three pieces shown in figure 6 each consists of only one type of curvature and so pieces are possible hole orbits and piece F9 is a possible electron orbit.

Figure 7 demonstrates the six basic pieces created by the overlaps of the high-frequency circles. The pieces are labelled as F1 (34.8 T), F2 (78.1 T), F3 (14.1 T), F4 (79.7 T), F5 (150.5 T) and F6 (324.3 T). Piece F4 (79.7 T) has uniform curvature and so is a hole orbit, whereas F1, F2, F3, F5 and F6 have mixed curvatures and therefore cannot be considered to be carrier orbits by themselves. However, by combining different combinations of these pieces, large carrier orbits can be formed. Figures 8–10 show sketches of some of the shapes of the uncoupled and coupled orbits from the high-frequency construction. These orbits correspond to the 178, 236, 264, 306, 401, 496, 725, 739, 875, 913 and 1199 T

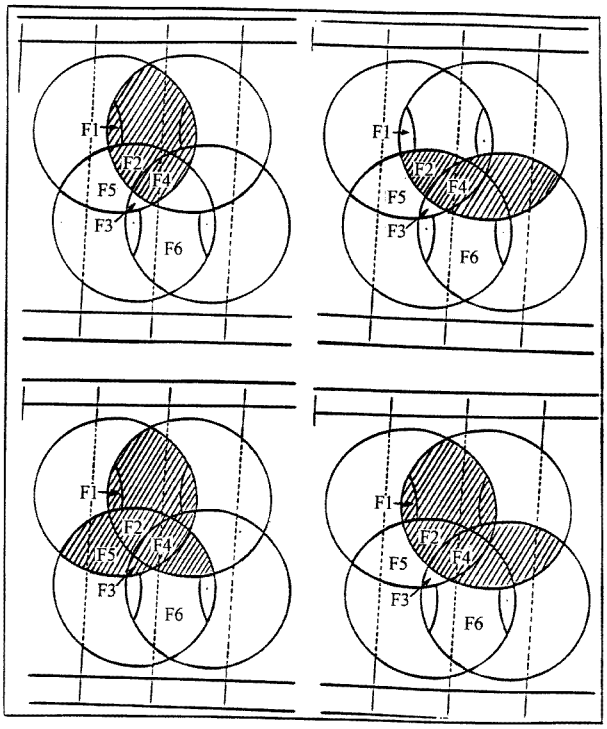

Figure 9. The circle construction showing coupled and uncoupled orbits (1106 T) corresponding to the 496, 401, 739 and 725 T frequencies.

frequencies. Table 2 presents an account of possible uncoupled and coupled orbits from the low- and high-frequency constructions. Some of these constructions may seem complicated as possible carrier orbits; however, all of the constructions are made up of the pieces in figure 7. The zone-folding model provides good identification for nearly all of the frequencies that are observed. However, there are other frequencies provided by the model that are not observed. There are four low frequencies predicted at 9.4, 11, 43.1 and 79 T that are not observed. These small orbits may not be detected by dHvA or may be shrunk to zero when a potential is included in the model. Also the fundamental frequency of 1106 T is not observed. This is not surprising since in this high-frequency band the orbits created by the zone-folding effect are dominant. In principle, there is an infinite number of orbits that can result from zone folding. At high frequencies the coupling of many small pieces results in a large number of possible orbits and clearly not all of them can be observed.

This zone-folding model does not include any interaction between the orbits. Interaction results in energy gaps at the intersections of orbits where there is degeneracy. These gaps have to be crossed by the assistance of magnetic breakdown. However, there is no direct evidence of breakdown since the same frequencies are observed at low and high fields and the relative Fourier-transform amplitudes are the same at low and high fields. Thus any breakdown takes place at low fields less than 2 T, indicating that the energy gaps are small.

Figure 11 shows the network of the zone folding resulting from different translations with reciprocal lattice vectors (b_1 and b_2) of the intercalant superlattice as a result of Bragg reflections for the high-frequency band 1106 T. The $(2\sqrt{1}83R26.33^\circ \times 4\sqrt{3}R0^\circ)$ superlattice

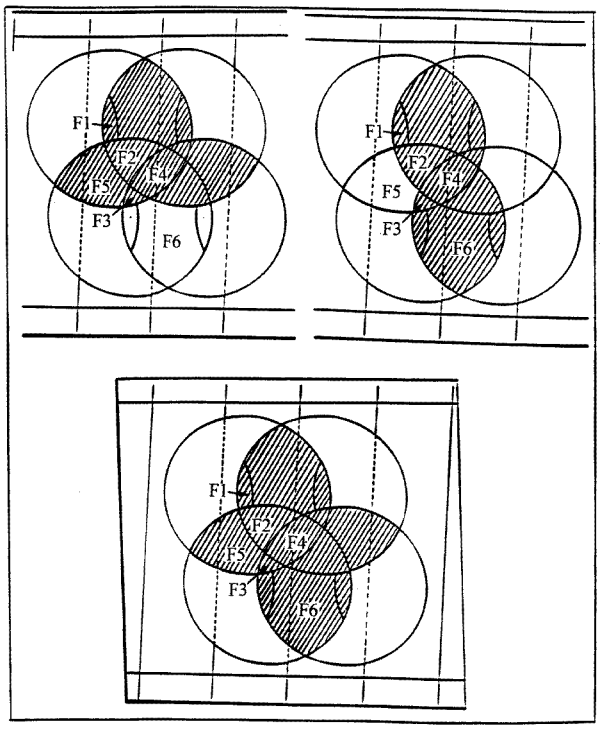

Figure 10. The circle construction showing coupled and uncoupled orbits (1106 T) corresponding to the 875, 913 and 1199 T frequencies.

allows for the reciprocal space translation of the cylindrical graphite Fermi surfaces located at the U and U′ points of the graphite Brillouin zone to the O and O′ points of the intercalant Brillouin zone. The ratio of magnitudes of reciprocal lattice vectors ($|b_1| = 0.6422$ Å^{-1} and $|b_2| = 0.1645$ Å^{-1}) of the intercalant superlattice is 3.91. It was observed that in general the coupled and uncoupled carried orbits resulting from translations with the shorter intercalant reciprocal lattice vector b_2 and from mixed translations (b_1 and b_2) produce oscillations with higher amplitudes. Circle constructions of 496 T—uncoupled orbit in figure 9—and of 913 T—coupled orbit in figure 10—are good examples of carrier orbits from b_2 translations. Circle constructions of coupled orbits in figure 8 are examples of carrier orbits resulting from mixed b_1 and b_2 translations. Also, the coupled and uncoupled carrier orbits resulting from translations with the long intercalant reciprocal lattice vector b_1 had low amplitudes and were often almost unobservable. They are also the ones which were not observed in samples 1–3.

In the experiment with sample 5 after exposure to air frequencies 322, 338, 357, 401, 431, 564, 590, 658 and 691 T were not observed in the dHvA spectrum or their amplitudes were too weak to be recorded. All of these frequencies, except frequency 590 T, correspond to the carrier orbits resulting from translations with the long intercalant reciprocal lattice vector b_1. Thus this periodicity is lost from the loss of IBr after air exposure.

The theoretical framework which incorporates experimental dHvA results and provides predictions for the Fermi level, charge transfer values and dispersion relations for acceptor GICs is provided by Blinowski *et al* [15]. The parameters in the model are the in-plane

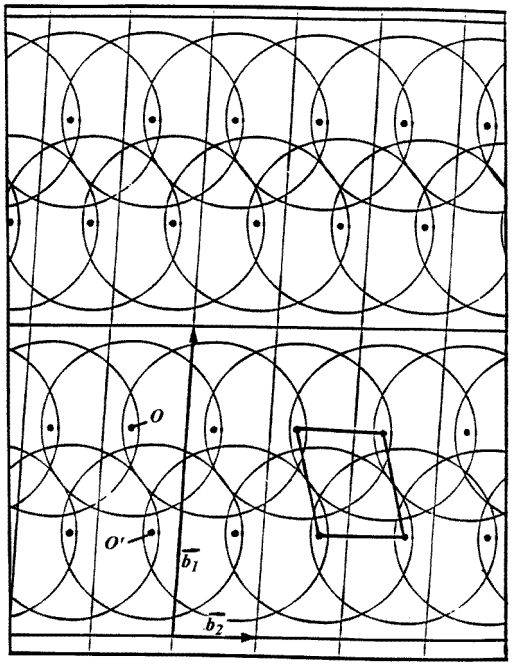

Figure 11. The network of the zone folding resulting from different translations with reciprocal lattice vectors (b_1 and b_2) of the intercalant ($2\sqrt{183}R26.33^\circ \times 4\sqrt{3}R0^\circ$) superlattice for the high-frequency band 1106 T.

interaction parameter γ_0, the first interplane interaction parameter γ_1 and the Fermi energy E_F. They were adjusted to fit the two basic frequencies $f_1 = 455$ T and $f_2 = 1106$ T. The corresponding experimental and calculated Fermi areas in units of Å^{-2} are 0.043 and 0.045 for f_1 and 0.106 and 0.108 for f_2. The model parameters are $\gamma_0 = 2.4$ eV, $\gamma_1 = 0.328$ eV and $E_F = -0.79$ eV. The charge transfer per intercalant molecule is 0.41 and the charge transfer per carbon atom f/l is 0.0197.

The model parameters are similar to those for other stage-2 acceptor GICs intercalated with $BiCl_3$, $SbCl_5$ and BF_4^- [14, 16] for which $\gamma_0 = 2.40$ eV and $\gamma_1 = 0.38$ eV from the Blinowski model. Thus the basic energy bands of all the stage-2 GICs are similar irrespective of whether there is zone folding.

It should be emphasized that the frequencies were explained by zone folding from the in-plane structure using only one adjustable parameter, the value of f_2, with the agreement shown in table 2. Thus an alternative explanation of the complicated data of figure 4 in terms of stage disorder is not likely. Also there is no evidence of stage disorder or mixed stages from x-ray diffraction (figure 1).

4. Conclusions

There are at least thirty frequencies in the dHvA spectrum of the stage-2 IBr GIC. The two Fermi surface cylinders of the graphite energy bands are translated by the $\sqrt{183}R26.33^\circ \times 2\sqrt{3}R0^\circ$ in-plane periodicity of the IBr structure. This results in overlaps of the Fermi surface and couples many carrier orbits. It dramatically demonstrates the effects

of two periodicities on the electronic properties. When the in-plane periodicity is reduced by exposing a sample to air, the translations by the larger reciprocal lattice vector are less effective in coupling the orbits.

This work demonstrates the sensitivity of the dHvA effect to internal periodicities. This is a sensitive effect. The Bragg reflection of electrons in the sample takes place and allows the translation by the reciprocal lattice vectors of the periodicity, which results in zone folding. In this way the dHvA effect becomes a very useful diffraction method. It clearly shows the in-plane periodicity of the IBr GIC. This is significant because most of the previous investigations [2–4] were made with the ICl GIC from which the periodicity of the IBr GIC was inferred. It is also very sensitive to the internal order which can be changed by air exposure even when the change is not detected by x-ray diffraction.

Acknowledgments

The research was supported by the Natural Sciences and Engineering Research Council of Canada. Technical and research assistance was provided by T Olech and J Palidwar. The x-ray analysis was carried out by W Gong of the Brockhouse Institute of Materials Research. The HOPG graphite was provided by Dr A W Moore.

References

[1] Selig H and Ebert L B 1980 *Adv. Inorg. Chem. Radiochem.* **23** 281
[2] Turnbull J A and Eeles W T 1966 *Proc. R. Soc. London* Series A **283** 63
[3] Wortmann G, Krone W, Kaindl G and Schlogl R 1988 *Synth. Met.* **23** 139
[4] Krone W, Wortmann G and Kaindl G 1989 *Synth. Met.* **29** F247
[5] Tiedtke M and Wortmann G 1989 *Synth. Met.* **34** 405
[6] Ohta Y, Kawamura K and Tsuzuku T 1986 *J. Phys. Soc. Japan* **55** 2338
[7] Ohta Y, Kawamura K and Tsuzuku T 1988 *J. Phys. Soc. Japan* **57** 196
[8] Tashiro K, Ozawa N, Sagihara K and Tsuzuku T 1990 *J. Phys. Soc. Japan* **59** 4022
[9] Kobayashi K, Oshima H, Sugihara K and Tsuzuku T 1994 *J. Phys. Soc. Japan* **63** 4451
[10] Tashiro K, Saito M and Tsuzuku T 1985 *Synth. Met.* **12** 63
[11] Marchesan D, Palidwar J D, Ummat P K and Datars W R 1996 *J. Phys.: Condens. Matter* **8** 991
[12] Datars W R, Palidwar J D, Chien T R and Ummat P K 1996 *Phys. Rev.* B **53** 1579
[13] Yosida Y and Tanuma S 1988 *Synth. Met.* **23** 199
[14] Zaleski H, Ummat P K and Datars W R 1987 *Phys. Rev.* B **35** 2958
[15] Blinowski J, Nguyen H H, Rigaux C, Vieren J P, Letoullec R, Furdin G, Herold A and Melin J 1980 *J. Physique* **41** 47
[16] Wang G, Ummat P K and Datars W R 1993 *Phys. Rev.* B **47** 3864